Bright Solid State Source of Photon Triplets

Milad Khoshnegar[1,2], Tobias Huber[3], Ana Predojević[3], Dan Dalacu[4], Maximilian Prilmüller[3], Jean Lapointe[4], Xiaohua Wu[4], Philippe Tamarat[5], Brahim Lounis[5], Philip Poole[4], Gregor Weihs[3], Hamed Majedi[1,2]

[1]*Department of Electrical and Computer Engineering, University of Waterloo, Waterloo, Ontario N2L 3G1, Canada*

[2]*Waterloo Institute for Nanotechnology, University of Waterloo, Waterloo, Ontario N2L 3G1, Canada*

[3]*Institut für Experimentalphysik, Universität Innsbruck, Technikerstr. 25, 6020 Innsbruck, Austria*

[4]*National Research Council of Canada, 1200 Montreal Road, Ottawa, Ontario K1A 0R6, Canada*

[5]*Université Bordeaux, LP2N Institut d'Optique and CNRS, Talence F-33405, France*

arXiv:1510.05898v2 [quant-ph] 3 Jun 2016

Producing advanced quantum states of light is a priority in quantum information technologies. While remarkable progress has been made on single photons and photon pairs, multipartite correlated photon states are usually produced in purely optical systems by post-selection[1–4] or cascading[5,6], with extremely low efficiency and exponentially poor scaling. Multipartite states enable improved tests of the foundations of quantum mechanics as well as implementations of complex quantum optical networks and protocols[3,7,8]. It would be favourable to directly generate these states using solid state systems, for better scaling, simpler handling, and the promise of reversible transfer of quantum information between stationary and flying qubits[9]. Here we use the ground states of two optically active coupled

quantum dots to directly produce photon triplets. The wavefunctions of photogenerated excitons localized in these ground states are correlated via molecular hybridization and Coulomb interactions[10]. The formation of a triexciton leads to a triple cascade recombination and sequential emission of three photons with strong correlations. The quantum dot molecule is embedded in an epitaxially grown nanowire engineered for single-mode waveguiding and improved extraction efficiency at the emission wavelength. We record 65.62 photon triplets per minute, surpassing rates of all earlier reported sources[5,6], in spite of the moderate efficiency of our detectors. Our structure and data represent a breakthrough towards implementing multipartite photon entanglement and multi-qubit readout schemes in solid state devices, suitable for integrated quantum information processing.

The most widespread technique for generating multipartite photon correlations relies on spontaneous parametric down conversion (SPDC) with low conversion efficiency[1,11] and restricted scalability, which limits its production rate and applications. In contrast, quantum dots offer the most practical route in building scalable quantum architectures and their efficiency reaches almost unity per excitation pulse, enabling high count rates. The ground state of a single quantum dot hosts at most two bright excitons[12], a biexciton, which can be controlled coherently[13] to produce correlated photon pairs. Thus creation of multipartite photon correlations in single quantum dots requires exploiting higher shells and phonon-mediated processes, which lead to poor photon correlation visibility and complicated excitation methods[14,15]. The coupled s shells of a quantum dot molecule (QDM), however, render additional excitonic states suitable for scaling up the number of correlated photons under present coherent schemes. A realization of photon triplets from a

triexciton forming in a QDM serves as an elementary step for direct generation of multiphoton entanglement, which has been so far limited to photon pairs in solid state systems[16].

Our QDM is composed of two $\mathrm{InAs}_x\mathrm{P}_{1-x}$ segments ($x \approx 0.15$ and 0.25) embedded inside an InP photonic nanowire that incorporates core and cladding regions[17] (Fig. 1a). The thick cladding of 250 nm in diameter aids funnelling the QDM emission into the fundamental HE_{11} mode[18] to be guided out toward the collection optics. The cladding is gently tapered (2°) at its apex to improve the photon extraction efficiency (Fig. 1b). The molecule contains two h_D $\sim$2.5-3 nm thick and D_NW $\sim$18 nm in diameter dots as confirmed by transmission electron microscopy (TEM) imaging (Fig. 1c). The growth of the second dot QD_R is seemingly influenced by the strain field caused by the formation of the first dot QD_L during the molecular beam epitaxy (MBE) process, giving rise to some compositional asymmetry of the molecule. Notice that even though the hybridization energy itself can exceed several tens of meV in strongly-coupled double dots[10], an important part of the s-shell splitting in the molecule studied here is induced by the above composition change. Such an inherent asymmetry aids the localization of the heavy hole wavefunctions mainly inside individual dots rather than evenly spreading throughout the molecule[19]. The proximity of dot and barrier compositions however leads to a comparatively weaker localization of the electron, and its orbital partially diffuses into the neighbouring dot. An interdot spacing of $\sim$8-10 nm was initially targeted in the vapour-liquid-solid (VLS) growth mode, however the Arsenic tailing in our dots possibly reduces the effective separation d down to $\sim$ 7 nm. Considering the low Arsenic concentration ($0.15 < x < 0.25$) of the dot segments, a thinner spacing would lift the barrier and aid delocalization of electrons, or would promote the directional nonresonant tunneling in the

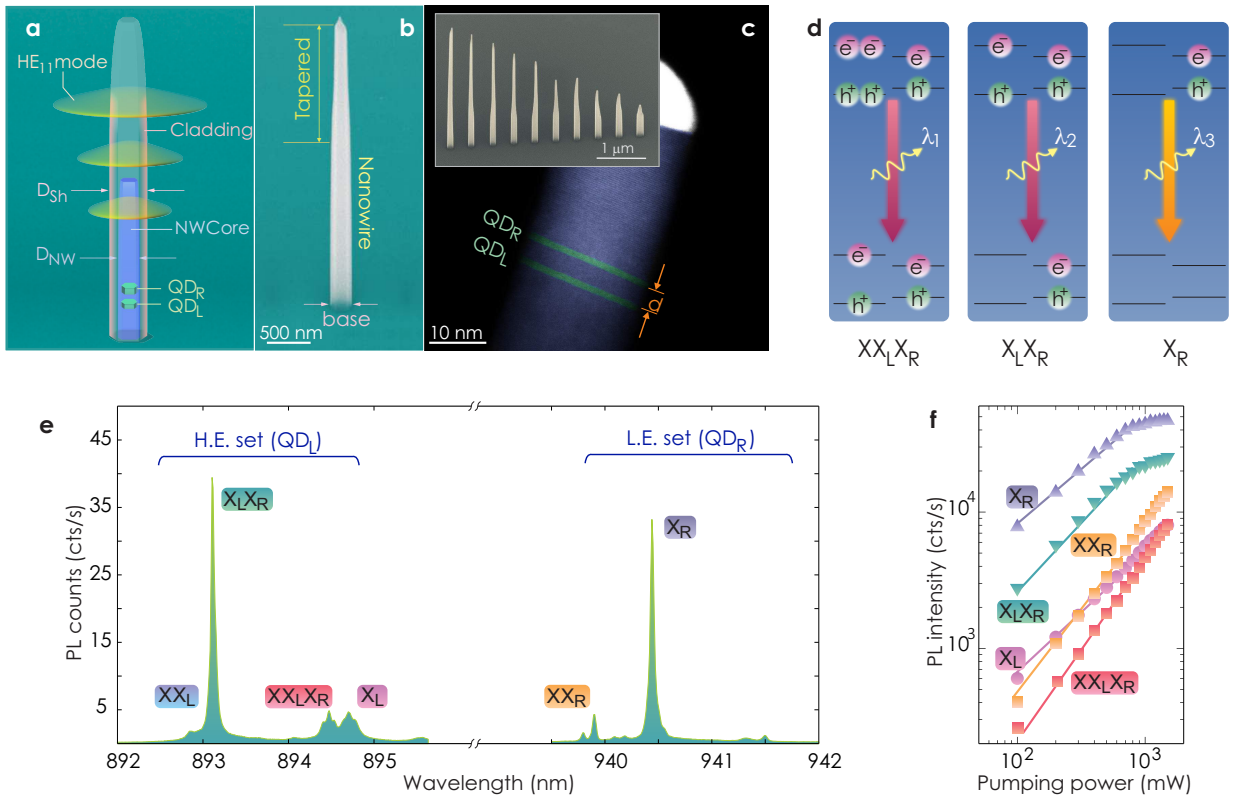

Figure 1: Structure and spectrum of Nanowire-QDM a) Schematic of QDM embedded inside a clad nanowire. The best suited nanowires consist of a thin core region $D_{\mathrm{NW}} = 18\text{-}20$ nm surrounded by a thick InP cladding (shell) $D_{\mathrm{Sh}} = 250$ nm that waveguides at least one principal optical mode at QDM emission wavelengths ∼894 and ∼940 nm. (b) False-coloured SEM image of a spatially isolated nanowire with hexagonal cross-section incorporating a single QDM. (c) False-coloured TEM image of an InP nanowire (core) grown on (111)B substrate in wurtzite phase embedding two In(As)P quantum dots separated by ∼7 nm. Inset: The nanowires are site-controlled allowing for excellent isolation of QDM spectrum from inhomogeneous broadening (d) Triple sequential transitions: carrier configurations of H.E. triexciton, separated biexciton and L.E. exciton. (e) Optical spectrum of QDM comprising two prominent features at ∼894 nm and ∼940 nm. Inset: PL intensity of the QDM resonances showing linear or superlinear dependence on the pump power.

QDM[20], whereas a larger spacing would impair the electron hybridization and interdot coupling.

In our experiment, the formation of a triexciton in the QDM entails the photongeneration of a biexciton (XX) in one quantum dot ($\mathrm{QD_L}$) along with an exciton (X) in the neighbouring dot ($\mathrm{QD_R}$) under continuous optical pumping. The predominant coupling mechanism among the two dots can be explained either via the wavefunction hybridization and Coulomb interactions[10,21], or the direct energy transfer of excitons (Förster process)[22], or nonresonant phonon-assisted tunneling. The direct transfer of exciton is caused by long-range Coulomb interactions and typically occurs within a few meV interdot energy splitting. As shown later, the energy detuning of the constituting quantum dots is several tens of meV in our molecule because of its structural asymmetry, hence the direct exciton transfer has a negligible impact on the interdot coupling here[22,23]. Moreover, the nonresonant tunneling of carriers in QDMs is a function of the phonon spectral density, thus depends on the wavefunction overlap and particularly the energy difference of the states involved in the transition. This implies that any carrier tunneling between the two detuned s shells of our QDM would require multiple acoustic phonon processes[24]. We will later demonstrate that nonresonant tunneling plays a minor role in the interdot communication here, and therefore wavefunction correlation is the primary source of coupling.

The studied QDM shows two distinguished high energy (H.E.) and low energy (L.E.) sets of spectral resonances at $\sim$894 nm and $\sim$940 nm corresponding to its molecular s-shell direct transitions (Fig. 1e). The formation probability of optically active "indirect excitons" should be small owing to the molecule asymmetry and rather single-dot-confined holes[25]. In addition to the

conventional exciton (X_{L} or X_{R}) and biexciton (XX_{L} or XX_{R}) direct transitions belonging to $\mathrm{QD_L}$ and $\mathrm{QD_R}$, there exist energy-shifted biexciton and exciton transitions, $XX_{\mathrm{L}}X_{\mathrm{R}}$ at $\lambda_1 = 894.5$ nm and $X_{\mathrm{L}}X_{\mathrm{R}}$ at $\lambda_2 = 893.1$ nm emerging due to Coulomb interaction with X_{R} at $\lambda_3 = 940.9$ nm. The carrier configuration related to the transitions creating the photon triplet are shown in Fig. 1d. They are assigned by acknowledging that bright interdot recombination is unlikely and that the $XX_{\mathrm{L}}X_{\mathrm{R}}$ and $X_{\mathrm{L}}X_{\mathrm{R}}$ resonances are located in the H.E. set. For simplicity, we name these two latter transitions "triexciton" and "separated biexciton", respectively. The power-dependent PL intensity of the above resonances exhibit the expected linear and superlinear regimes for both series of regular and energy-shifted excitons and biexcitons, respectively (Fig. 1f). The emergence of X_{R} at the lowest excitation levels makes the conditional formation of separated biexciton and triexciton in $\mathrm{QD_L}$ more likely than that of X_{L} and XX_{L}. XX_{L} grows on the shoulder of the neighbouring $X_{\mathrm{L}}X_{\mathrm{R}}$ resonance at higher excitation levels, which hinders resolving its power dependence over the entire range.

In order to understand the possible effect of nonresonant carrier tunneling, we performed a time-resolved micro-PL experiment on the present QDM and another double dot, $\mathrm{DD_2}$, with identical single dot specifications, but an increased interdot spacing of over 30 nm in $\mathrm{DD_2}$ to eliminate the coupling. The lifetime of the single exciton X_{L} of the QDM was measured $\sim 2.8 \pm 0.2$ ns (similar value can be inferred by comparing $X_{\mathrm{L}}X_{\mathrm{R}}$ and X_{R} lifetimes as shown in Supporting Information), whereas the same X_{L} resonance of $\mathrm{DD_2}$ lasted $\sim 2.5 \pm 0.2$ ns. In general, the decay time τ_d of the exciton X_{L} in a molecule, where nonresonant tunneling from $\mathrm{QD_L}$ to $\mathrm{QD_R}$ continuously takes place, is given by $1/\tau_d = 1/\tau_r + 1/\tau_t$, where τ_r is the exciton radiative lifetime and $1/\tau_t$ is the

tunneling rate. The fact that τ_d ($= 2.8 \pm 0.2$ ns) and τ_r ($= 2.5 \pm 0.2$ ns) are comparable within the accuracy of our experiment suggests that the impact of nonresonant tunneling between the s shells of our QDM is negligible and perhaps a reverse mechanism exists between the s shell of $\mathrm{QD_L}$ and the nearby d shells of $\mathrm{QD_R}$ appearing at slightly higher energies in the spectrum. The nonresonant electron tunneling is however enhanced at a small enough spacing ($d < 3$ nm), where the barrier is lifted and $\mathrm{QD_L}$ is steadily emptied showing weak PL intensity (see Supporting Information). The above observation indicates that the coupling in our QDM forms primarily via the hybridization of electron wavefunctions.

We conducted magneto-optical experiments to identify the resonances by comparing their Zeeman splitting to the theoretically predicted values. A bright exciton such as X_R comprises a spin doublet $|S_{X_\mathrm{R},||}\rangle = \{|+1\rangle = |\downarrow\Uparrow\rangle, |-1\rangle = |\uparrow\Downarrow\rangle\}$ which splits by $\Delta_{X_\mathrm{R}} = g_{X_\mathrm{R},||}\,\mu_\mathrm{B}\,B_{||}$ in Faraday configuration (magnetic field $B_{||}$ applied along the nanowire axis), where $\downarrow\uparrow$ ($\Downarrow\Uparrow$) represents the electron (heavy hole) spin, $g_{X_\mathrm{R},||} = g_{e_\mathrm{R},||} + g_{h_\mathrm{R},||}$ is the axial exciton g-factor and μ_B is the Bohr magnetron. A regular biexciton has zero spin, thus its transition to the exciton state experiences the same splitting. The interdot biexciton $X_\mathrm{L}X_\mathrm{R}$ is however fourfold degenerate $|S_{X_\mathrm{L},||}, S_{X_\mathrm{R},||}\rangle = \{|\pm1, \pm1\rangle\}$ at $\mathbf{B} = 0$ with four bright decay channels down to the X_R doublet, $|1, \pm1\rangle \rightarrow |\pm1\rangle$ and $|-1, \pm1\rangle \rightarrow |\pm1\rangle$, if spin flip processes[26] are ruled out. These decay channels split into two doublets spaced by $\Delta_{X_\mathrm{L}X_\mathrm{R}} = g_{X_\mathrm{L},||}\,\mu_\mathrm{B}\,B_{||}$. Finally, the triexciton produces a bright spin doublet $|S_{XX_\mathrm{L},||}, S_{X_\mathrm{L}X_\mathrm{R},||}\rangle = \{|0, \pm1\rangle\}$ which decays via two doubly degenerate transitions to the separated biexciton, $|0, \pm1\rangle \rightarrow |1, \pm1\rangle$ and $|0, \pm1\rangle \rightarrow |-1, \pm1\rangle$, with $\Delta_{XX_\mathrm{L}X_\mathrm{R}} = g_{X_\mathrm{L},||}\,\mu_\mathrm{B}\,B_{||}$ energy splitting. We investigated the QDM PL under magnetic field in the Faraday configuraion

(not shown here) and a tilted ($\theta = 12^\circ$) configuration (Fig. 2a). The Zeeman coupling of the bright and dark spin states should cause a fourfold splitting of the fine structure in charged excitons should occur even at small magnetic fields in the tilted configuration, whereas the intrinsic dark-bright splitting in neutral excitons prohibits such mixing except for high field magnitudes[27]. Observation of dual splittings in the tilted configuration would therefore imply that the resonances do not originate from charged states. The PL intensity versus magnetic field B_θ and wavelength is shown in Fig. 2b, where the dashed lines indicate the evolution of the resonances. The H.E. set is displayed in higher pumping levels ($P_2 = 10P_1$) well above the onset of the triexciton emission. We fit the spectral peak displacement with $\pm g_{X,\theta}\,\mu_B\,B_\theta + \gamma_{X,\theta}\,B_\theta^2$ to remove the diamagnetic shift ($\propto B_\theta^2$) present in the weak-field regime[28], and obtain $g_{X_\mathrm{R},\theta} = -0.92$ and $\gamma_{X_\mathrm{R},\theta} = 8.30\ \mu\mathrm{eV/T^2}$ for the L.E. exciton and $g_{X_\mathrm{L}X_\mathrm{R},\theta} = -1.62$ and $\gamma_{X_\mathrm{L}X_\mathrm{R},\theta} = 11.94\ \mu\mathrm{eV/T^2}$ for the separated biexciton. The spectra and corresponding Zeeman splittings of the $X_\mathrm{L}X_\mathrm{R}$ (and $XX_\mathrm{L}X_\mathrm{R}$) doublets along with X_R (and XX_R) singlets at $B_\theta = 2.5\ \mathrm{T}$ are shown in Figs. 2c-d, verifying that $\Delta_{XX_\mathrm{L}X_\mathrm{R}} = \Delta_{X_\mathrm{L}X_\mathrm{R}}$ and $\Delta_{XX_\mathrm{R}} = \Delta_{X_\mathrm{R}}$.

The next step was to measure the second-order autocorrelation function[29] of each individual resonance and the cross-correlation functions[12] $g^{(2)}_{\alpha\beta}(\tau)$ between various pairings (α,β) of distinct resonances ($\tau_{\alpha\beta} = t_{D\alpha} - t_{D\beta}$ denotes the delay time between photon detections). These correlations can provide insight into the coupling strength and the nature of the lines[30]. An autocorrelation experiment on every QDM resonance in our sample verified their low multiphoton emission probability by featuring an antibunching dip at $\tau = 0$. Among all possible cross correlations of QDM resonances, the ones measured between $XX_\mathrm{L}X_\mathrm{R}$, $X_\mathrm{L}X_\mathrm{R}$, and X_R are of highest interest

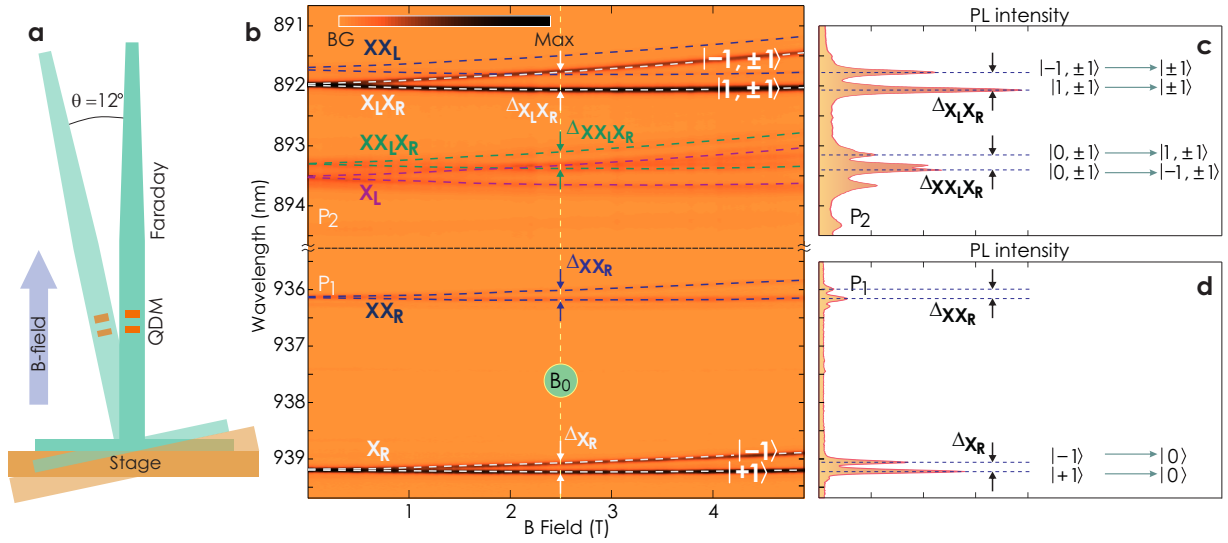

Figure 2: Magneto-PL and Zeeman splitting of QDM resonances a) Schematic of nanowire-QDM in magnetic field in Faraday and tilted ($\theta = 12°$) orientations. (b) QDM PL intensity versus tilted magnetic field B_θ. The L.E. set is measured at $P_1 = 0.5\ \mu$W and shows two prominent doublets. The H.E. set is scanned at $P_2 = 10P_1$ where the triexciton spin splitting becomes visible with respect to background light. (c-d) Spectra of H.E. and L.E. sets measured at $B_0 = 2.5$ T as highlighted by the yellow dashed line in (b). The doublet and singlet transitions under investigation are labelled with their associated spin states for further clarity. The biexciton transitions in each set, either shifted or unshifted, mirror their corresponding exciton transitions, $\Delta_{XX_LX_R} = \Delta_{X_LX_R}$ $(= \Delta_{X_L})$ and $\Delta_{XX_R} = \Delta_{X_R}$.

for the photon triplet characterization. A triplet state comprising temporally correlated photons $|\lambda_1\lambda_2\lambda_3\rangle$ originates from a triple sequential cascade in the QDM (Fig. 1d). In our correlation setup illustrated in the Supporting Information, a diffraction grating separates the $XX_{\mathrm{L}}X_{\mathrm{R}}$, $X_{\mathrm{L}}X_{\mathrm{R}}$, and X_{R} photons towards the detectors D1, D2 and D3. All cross-correlations $g^{(2)}_{\alpha\beta}(\tau)$ of the above three resonances feature an asymmetric bunching-antibunching behaviour[12] as expected for cascade transitions (Figs. 3a-c). The cross-correlations between $XX_{\mathrm{L}}X_{\mathrm{R}}$ ($X_{\mathrm{L}}X_{\mathrm{R}}$) and X_{R} are fitted with $g^{(2)}_{\mathrm{fit}}(\tau) = 1 - ae^{(\tau/\tau_{\mathrm{fit}})}$ ($\tau < 0$) resulting in $g^{(2)}_{\mathrm{fit}}(0^-) = 0.71$ (0.59) considerably smaller than unity, which indicates that the system is indeed a molecule rather than two separate dots. Similarly, the cross correlations among the remaining L.E. and H.E. resonances featured above antibunching characteristic, in contrast to cross correlations in DD2 which showed no sign of antibunching.

In order to prove that the QDM actually emits a photon triplet, we conducted a triple coincidence experiment[31] by sending detector pulses D1 (as Start), D2 (as Stop1) and D3 (as Stop 2) into a time-tagging device. The time-resolved histogram versus τ_{21} and τ_{31} features a fully random contribution due to uncorrelated photons (319 counts) along with three contributions each coming from two correlated photons and the third being accidental resulting in a total level of (partially correlated) triple events of 618.6 counts. We observe a large number of threefold coincidences in the vicinity of zero time delay (Fig. 3d) above the partially correlated events. We record 20744 photon counts in total (including 8932 background counts) integrated in 3 hours in the coincidence window of $\tau_{21} \in \{-0.768, 1.28\}$ ns and $\tau_{31} \in \{-1.28, 2.304\}$ ns (see Fig. 3e). After subtracting the background, caused by either random or partially correlated events, we are left with 11812 photon triplets corresponding to an average detection rate of 65.62 triplets per minute. We estimate

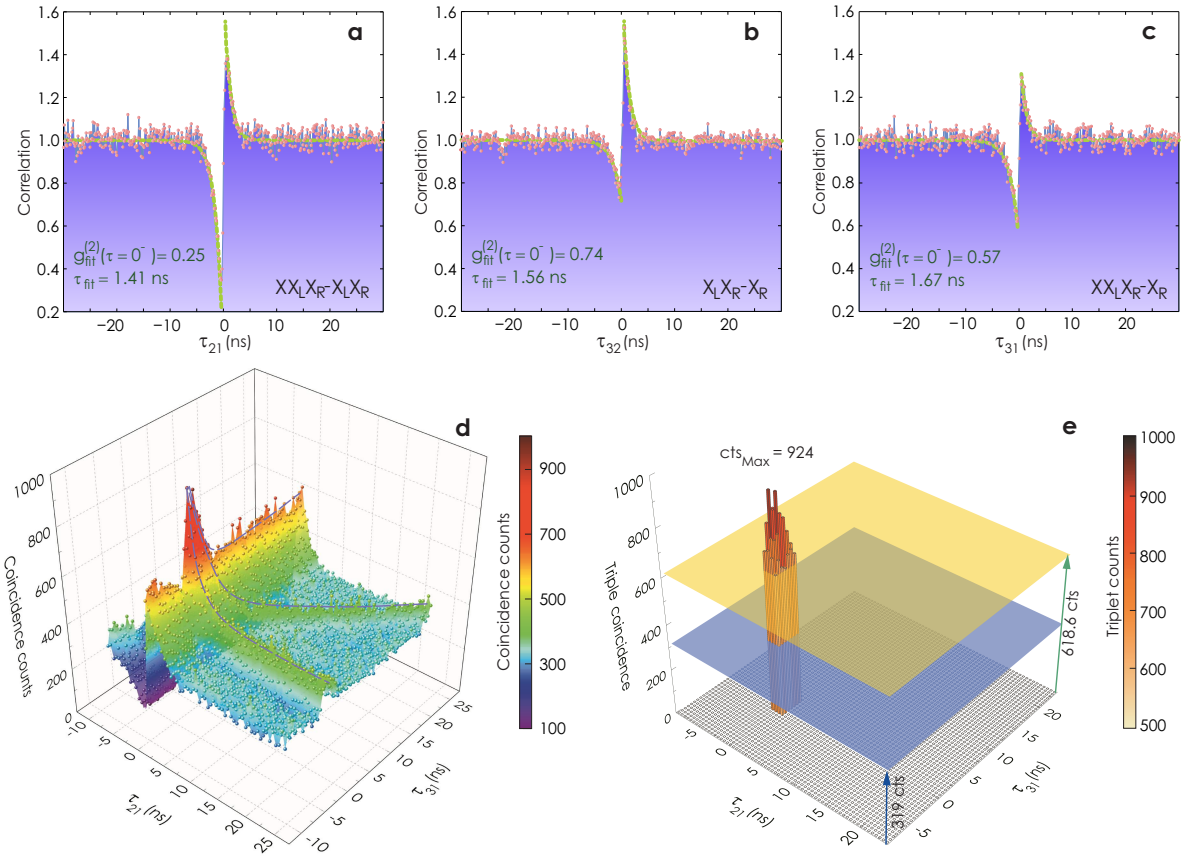

Figure 3: Dual-channel cross correlations and triple coincidence histogram (a-c) Normalized cross correlations of X_{R}, $X_{\mathrm{L}}X_{\mathrm{R}}$ and $XX_{\mathrm{L}}X_{\mathrm{R}}$ versus delay time measured at the high excitation power density (PD) of 6.9 $\mathrm{W/mm^2}$ showing a sequential triple cascade recombination. (d) The triple coincidence histogram (total recording time 3 h) was measured at $\mathrm{PD} = 460\,\mathrm{mW/mm^2}$ and is plotted versus τ_{21} and τ_{31}, linearly interpolated with a color-mapped surface. The threefold coincidence peak near the origin signifies the strong temporal correlations of the emitted photons. e) Events above the two-fold cascade threshold from d) without interpolation. The threshold level (yellow plane) was determined as the (peak) value of $g^{(2)}_{21}(0^+)$ averaged over t_{D3} outside the triple coincidence window. For comparison the expected level of accidental triplet events is shown in blue.

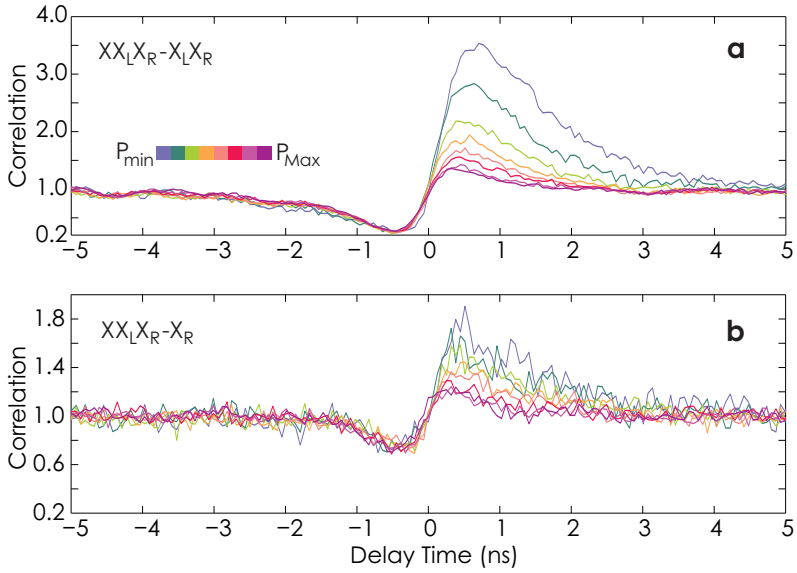

Figure 4: Dependence of bunching visibility on the excitation power in a triple cascade (a-b) Normalized cross correlations of $XX_{\mathrm{L}}X_{\mathrm{R}}$ resonance with $X_{\mathrm{L}}X_{\mathrm{R}}$ and X_{R} resonances measured at eight distinct power densities increasing quadratically from 220 $\mathrm{mW/mm^2}$. The histograms are color-coded according to the applied pumping levels.

that only 0.15% of all photon triplets could be detected because of the low detection efficiency of our detectors, $\eta_{\mathrm{D}} = \eta_{\mathrm{D1}}\ \eta_{\mathrm{D2}}\ \eta_{\mathrm{D3}}$ ($\eta_{\mathrm{D1}} = 25\%$, $\eta_{\mathrm{D2}} = 25\%$ and $\eta_{\mathrm{D3}} = 15\%$ at the respective wavelengths), along with non-ideal extraction efficiency ($\eta_{\mathrm{C}} = 25\%$ at $D_{\mathrm{Sh}}/\lambda = 0.21$[32]), fibre coupling efficiency ($\eta_{\mathrm{F}} = 85\%$) and grating efficiency ($\eta_{\mathrm{G}} = 75\%$). The above photon triplet rate is, to the best of our knowledge, the highest recorded rate exceeding the value of 11.1 per min reported for direct generation of photon triplets via cascaded SPDC[6].

In general, the bunching peak $g^{(2)}_{\alpha\beta}(0^+)$ of a cascade decreases with the excitation rate, because the ratio of true cascade events versus individual excitations becomes less favorable, as has been observed in regular biexciton-exciton cascades of single quantum dots[33]. We examined this behavior by applying increasing levels of pump power while recording the cross correlations be-

tween the triexciton and the other two resonances (see Fig. 4). The measurements were conducted in a regime where the resonance PL intensity to background hardly changed, thus the variation in the bunching peak was mainly a function of the ratio between the excitation rate and transition lifetimes. The suppression of bunching visibility agrees with the results of our theoretical model based on the time propagation matrix method[30], as explained in the Supporting Information, and reconfirms the cascaded nature of the selected transitions.

In conclusion, we have demonstrated that a triexciton bound in a QDM can originate time-ordered photon triplets in a cascaded process. The present source is brighter than any existing source in terms of triplet generation rate. We expect to improve this rate by reducing the inter-dot energy splitting, deterministic coherent pulsed excitation of the triexciton to reduce the background, enhanced collection efficiency and the use of more efficient detectors. A triexciton forming in the s shells of a QDM benefits from far better coherence properties than the p-shell triexcitons[15] in single quantum dots because it does not involve any phonon assisted transisions. It can therefore be deterministically controlled via resonant pumping for generating Greenberger-Horne-Zeilinger[1] (GHZ) and W[34] states entangled in either polarization[17] or time-bin[13]. With the earlier demonstration of quantum-dot-based quantum key distribution (QKD)[35], our device opens new avenues toward implementation of multiparty quantum secret sharing on integrated semiconductor chips.

Methods

Nanowire-QDM Fabrication

The InP nanowires with embedded In(As)P quantum dots are grown using selective-area VLS epitaxy. The nanowires are grown on a SiO_2-patterned (111)B InP substrate. The pattern consists of circular holes defined using electron-beam lithography and hydrofluoric acid wet-etch. A single gold particle is deposited in each hole using a self-aligned lift-off process, with the size of the particle determined by the hole size and the thickness of deposited gold. We employ chemical beam epitaxy (CBE) with trimethylindium (TMI) and pre-cracked PH_3 and AsH_3 sources. The growth temperature is $420°$C. Two growth modes are utilized to grow (i) a nanowire core, which defines the quantum dots, and (ii) a shell, which defines the cladding of photonic nanowire. The nanowire core is grown under a reduced PH_3 flow resulting in an untapered InP nanowire with a diameter corresponding to the gold catalyst particle, approximately 20 nm in this work. The nanowires are pure phase wurtzite with less than 1 stacking fault per micron[36]. The double In(As)P quantum dots are grown by switching the group V species from phosphorous to arsenic to grow the first dot, switching back to phosphorous to grow the InP spacer, then switching back to arsenic to grow the second dot while maintaining a constant flux of TMI. Samples were grown with quantum dot growth times of 2.5 and 3 seconds, and with spacer times of 10, 15, and 60 seconds. The interdot spacing for a given growth time between dots depends on the core diameter due to a diameter-dependent growth rate[37]. By using a diameter-dependent growth model[37] we calculate an interdot separation of 8-20 nm for core diameters of 18-24 nm. Details of the spacer-dependent interdot coupling are beyond the scope of this work and will be published elsewhere. The spacer of QDM

studied here is 10 seconds ($\sim$ 7-8 nm) that provides the optimum coupling. The nanowire shell is grown by increasing the PH_3 flow rate by a factor of three, which reduces the Indium adatom migration length and promotes deposition on the nanowire sidewall facets. The shell is grown to reach base diameters of 250 nm, resulting in nanowires with heights of ~ 5 μm and tapers of $\sim 2^{\circ}$.

Optical Experiments

The sample is cooled down to 6 K in a customized and thermally stabilized liquid-Helium continuous-flow cryostat. The QDM is nonresonantly excited either by a cw or a ps-pulsed Ti:Sapphire laser at 820 nm with 8.4 ps pulse duration (80 MHz repetition rate) slightly above the wurtzite InP band gap 1.49 eV (832 nm) and the donor-acceptor recombination level 1.44 eV (861 nm). We excite the QDM via a separate objective rather than the collecting objective even though this is not reflected in the setup schematic in Supporting Information. The molecule luminescence is collected using an objective lens with numerical aperture (NA) of 0.7 and dispersed by grating monochromators with spectral resolution of $\sim$0.01 nm to split the spectral lines and send the respective photons into separate avalanche photodiodes (APD). APDs are identical with $\sim$300 ps temporal resolution and $\sim 25\%$ ($\sim 15\%$) detection efficiency at 893 nm (940 nm). The combination of spectrometer and charge coupled device (CCD) camera enables performing in-situ spectroscopy during the recording of counts in the correlation measurement setup (composed of APDs and ps time-tagging module). Only two APDs register the photon counts to conduct the autocorrelation and the conventional dual-channel cross correlation analysis, whereas all the three APDs are in use for the triple coincidence experiment. In the dual-channel correlation measurements, the H.E. set resonances are cross correlated utilizing two 5 micron core optical fibres for photon collection. In the triple coin-

cidence experiment, we collected from the L.E. set using a single mode fibre with 9 micron core optimized for telecommunication wavelength, that operates as a multimode fibre at 940 nm. The multimode character improves the collection efficiency without the requirement for an optimized mode matching. However, owing to the small core radius the background light picked up from X_{R} is suppressed and the antibunching dip in triple coincidence histogram is improved compared to a 125 m core multimode fiber. To produce the power-dependent cross correlation histograms in cw excitation mode, we started from 220 $\mathrm{mW/mm^2}$ (with 4 $\mu\mathrm{m}$ spot size and excitation objective tilted 22° from the optical table axis) and raised the pump power thus to linearly increase the shifted biexciton $XX_{\mathrm{L}}X_{\mathrm{R}}$. Therefore the pump power scales up approximately in a quadratic fashion until the $X_{\mathrm{L}}X_{\mathrm{R}}$ resonance is saturated. In order to resolve the associated lifetimes, the QDM is heavily pumped within each pulse using the Ti:Sapphire laser in a way that its resulting spectrum exactly resembles the one under cw excitation. For magneto-optical measurements the setup remains unchanged except that the cryostat is replaced by a continuous flow exchange gas cryostat with a 7 T split-pair superconducting magnet. The QDM is excited co-linear to the collection through the collection objective with a Ti:Sapphire laser. For the mixed Voigt-Faraday (tilted) configuration the sample is rotated 12° inside the cryostat.

Author Contribution

M.K. conceived the idea and developed the theory. M.K. and D.D. designed the QDM. D.D., J.L., X.W. and P.P. fabricated the nanowire-QDMs. M.K., A.P and T.H. designed the photon statistics experiments. T.H., A.P. and M.P. accomplished the photon correlation measurements.

M.K., A.P., and B.L. designed the magneto-optical measurements conducted by A.P., P.T., and M.P. T.H., A.P. and M.P. compiled the data and M.K. carried out the data analysis and wrote the manuscript with feedback from all co-authors. G.W. and H.M. supervised the project and contributed to the manuscript.

Acknowledgement

This work was funded by NSERC Discovery Grant Program, National Research Council Canada and the European Research Council. M.K. thanks NSERC for partial support through the CryptoWorks21 fellowship. T.H. thanks the Austrian Academy of Sciences for receiving a DOC Fellowship. A.P. would like to thank the Austrian Science Fund for the support provided through project number V-375. P.T. and B.L. acknowledge financial support from the Institut Universitaire de France and the Laphia cluster of excellence (IDEX Bordeaux).

Author Information

Corresponding Author: contact M.K. (m3khoshn@uwaterloo.ca)

Supporting Information

Interdot coupling versus spacing We performed a PL spectroscopy measurement on an ensemble of nanowire-embedded QDMs. Low excitation powers were applied to avoid the activation of multiexciton complexes. The dependence of the exciton resonance associated with each dot, X_{R}

and X_{L}, on the interdot spacing is plotted in Fig. 5. Since the spacing is a function of both the QDM diameter and the growth time (see Methods), the diameter-dependent shifts of the X_{R} and X_{L} resonances are removed in order to give better insight into the effect of spacing on hybridization. The spacing values shown here are nominal values d_{n} intended during the growth process and the effective interdot spacings d_{eff} are smaller as explained within the main text. At a constant pump power, we consistently noticed the decrease in the PL intensity of the H.E. set (or X_{L}) by reducing the spacing until it almost disappeared for the nominal spacing of $d_{\mathrm{n}} \sim 5.5$ nm ($d_{\mathrm{eff}} \sim 3$ nm). This indicates the direct electron tunneling from the "smaller" dot into the "larger" dot occurs with tunneling rates higher than the exciton decay rate in the smaller dot at such interdot spacing. For a large spacing, for example $d_{\mathrm{n}} > 18$ nm, an energy separation of at most 50 meV exists between the two resonances, which originates from structural asymmetry. However, for smaller spacing $d_{\mathrm{n}} < 18$ nm, the energy separation increases, partly because of the stronger hybridization energy of the QDM. This proves that at the spacing of $d_{\mathrm{n}} \sim 10$ nm ($d_{\mathrm{eff}} \sim 7$ nm) (corresponding to the QDM studied in the main text), the wavefunction hybridization and Coulomb interactions result in the coupling of the two quantum dots.

Measurement setup We use either cw or pulsed Ti:Sapphire laser to pump the QDM depending on the nature of experiment as described in Methods. The emission of cryogenically cooled nanowire-QDM is either sent to the spectroscopy module, composed of spectrometer and CCD, or photon statistics module, composed of gratings for dispersing photons and correlation setup (APDs and time-tagging card) for recording the correlation histogram. To resolve triple coincidence counts, photons from $XX_{\mathrm{L}}X_{\mathrm{R}}$, $X_{\mathrm{L}}X_{\mathrm{R}}$ and X_{R} are sent to three identical APDs (D1-D3). The

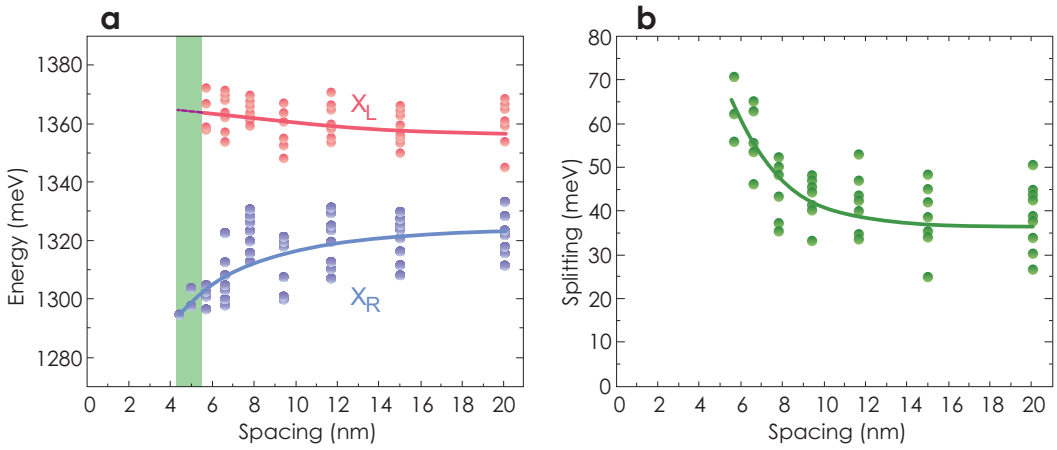

Figure 5: (a) The evolution of the QDM exciton energies as a function of the nominal interdot spacing d_{n}. The green-shaded area determines where the H.E. PL intensity becomes weak. (b) Energy splitting of the H.E. and L.E. sets versus the nominal interdot spacing.

polarization module, composed of quarter wave plate (QWP), half wave plate (HWP) and polarizer (Pol) is employed to measure fine structure splittings.

Cross-correlation curves and bunching visibility To calculate the temporal correlations, we present a numerical model incorporating the energy levels along with the pumping and decay rates of important transitions. The model includes eight energy states $|G\rangle$, $|X_{\mathrm{L}}\rangle$, $|X_{\mathrm{R}}\rangle$, $|XX_{\mathrm{L}}\rangle$, $|X_{\mathrm{L}}X_{\mathrm{R}}\rangle$, $|XX_{\mathrm{R}}\rangle$, $|XX_{\mathrm{L}}X_{\mathrm{R}}\rangle$ and $|X_{\mathrm{L}}XX_{\mathrm{R}}\rangle$, as illustrated in Fig. 7. The three primary transitions scrutinized in the main text are highlighted with thick coloured arrows. We limit our Hilbert space up to the triexciton level because the formation of higher states is unlikely at the applied pump powers and their effect on temporal characteristics of desired resonances is trivial.

The diagram plotted in Fig. 7 can be represented in an 8×8 time propagation matrix expanded on $\vec{V} = |G\ \ X_{\mathrm{L}}\ \ X_{\mathrm{R}}\ \ XX_{\mathrm{L}}\ \ X_{\mathrm{L}}X_{\mathrm{R}}\ \ XX_{\mathrm{L}}X_{\mathrm{R}}\ \ XX_{\mathrm{R}}\ \ X_{\mathrm{L}}XX_{\mathrm{R}}\rangle^{\mathrm{T}}$ where $d\vec{V}/dt = \mathbf{M}\vec{V}$:

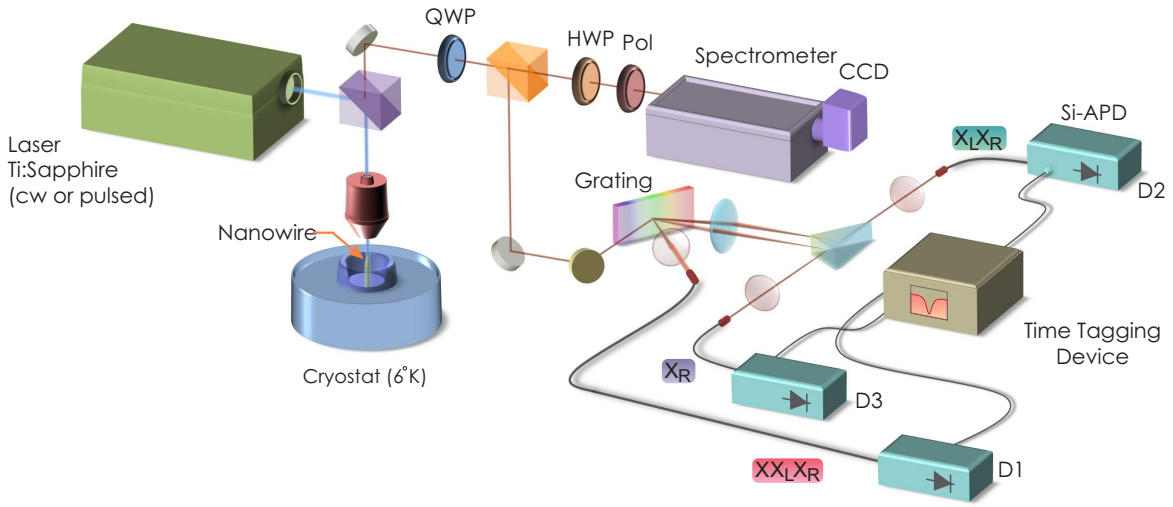

Figure 6: Simplified optical setup used for the correlation measurements

$$\mathbf{M} = \begin{pmatrix} -\mathrm{W}_{\mathrm{x}}^{\mathrm{L}} - \mathrm{W}_{\mathrm{x}}^{\mathrm{R}} & \Gamma_{\mathrm{L}} & \Gamma_{\mathrm{R}} & 0 \\ \mathrm{W}_{\mathrm{x}}^{\mathrm{L}} & -\mathrm{W}_{\mathrm{xx}}^{\mathrm{L}} - \mathrm{W}_{\mathrm{x}}^{\mathrm{R}} - \mathrm{W}_{\mathrm{T}} - \Gamma_{\mathrm{L}} & 0 & 2\Gamma_{\mathrm{L}} \\ \mathrm{W}_{\mathrm{x}}^{\mathrm{R}} & \mathrm{W}_{\mathrm{T}} & -\mathrm{W}_{\mathrm{xx}}^{\mathrm{R}} - \mathrm{W}_{\mathrm{x}}^{\mathrm{L}} - \Gamma_{\mathrm{R}} & 0 \\ 0 & \mathrm{W}_{\mathrm{xx}}^{\mathrm{L}} & 0 & -\mathrm{W}_{\mathrm{x}}^{\mathrm{R}} - 2\Gamma_{\mathrm{L}} - 2\mathrm{W}_{\mathrm{T}} \\ 0 & \mathrm{W}_{\mathrm{x}}^{\mathrm{R}} & \mathrm{W}_{\mathrm{x}}^{\mathrm{L}} & 2\mathrm{W}_{\mathrm{T}} \\ 0 & 0 & 0 & \mathrm{W}_{\mathrm{x}}^{\mathrm{R}} \\ 0 & 0 & \mathrm{W}_{\mathrm{xx}}^{\mathrm{R}} & 0 \\ 0 & 0 & 0 & 0 \end{pmatrix}$$

$$
\begin{pmatrix}
0 & 0 & 0 & 0 \\
\Gamma_{\mathrm{R}} & 0 & 0 & 0 \\
\Gamma_{\mathrm{L}} & 0 & 2\Gamma_{\mathrm{R}} & 0 \\
0 & \Gamma_{\mathrm{R}} & 0 & 0 \\
-\mathrm{W_T} - \mathrm{W_{xx}^L} - \mathrm{W_{xx}^R} - \Gamma_{\mathrm{L}} - \Gamma_{\mathrm{R}} & 2\Gamma_{\mathrm{L}} & 0 & 2\Gamma_{\mathrm{R}} \\
\mathrm{W_{xx}^L} & -2\Gamma_{\mathrm{L}} - \Gamma_{\mathrm{R}} - 2\mathrm{W_T} & 0 & 0 \\
\mathrm{W_T} & 0 & -\mathrm{W_x^L} - 2\Gamma_{\mathrm{R}} & \Gamma_{\mathrm{L}} \\
\mathrm{W_{xx}^R} & 2\mathrm{W_T} & \mathrm{W_x^L} & -2\Gamma_{\mathrm{R}} - \Gamma_{\mathrm{L}}
\end{pmatrix} \tag{1}
$$

.

The time evolution of $\vec{V}$ is obtained by diagonalizing **M**, $\mathbf{M} = \mathbf{P\Lambda P}^{-1}$, and $\vec{V(t)}$ is given by $\vec{V(t)} = \mathbf{U}(t)\vec{V(0)}$, where $\mathbf{U}(t)$ is the unitary time evolution operator $\mathbf{U}(t) = \mathbf{P}e^{\mathbf{\Lambda}t}\mathbf{P}^{-1}$. Here $\mathrm{W_x^L}$ ($\mathrm{W_x^R}$) is the pumping rate of the exciton in the smaller (larger) dot. We assume that when the s shell is already occupied with an exciton, the effective pumping rate to form the second exciton ($\mathrm{W_{xx}^L}$, $\mathrm{W_{xx}^R}$) is lower. Γ_{L} (Γ_{R}) here is the recombination rate of an exciton in the smaller (larger) quantum dot. To extract Γ_{L} and Γ_{R} from the time-resolved PL experiments, we averaged over the $X_{\mathrm{L}}X_{\mathrm{R}}$ and X_{R} lifetimes measured at eight increasing pump powers and used the following relations: $\Gamma_{\mathrm{R}} = \Gamma_{X_{\mathrm{R}}} = 0.58\ (\mathrm{ns})^{-1}$, $\Gamma_{\mathrm{L}} = \Gamma_{X_{\mathrm{L}}X_{\mathrm{R}}} - \Gamma_{\mathrm{R}} = 0.32\ (\mathrm{ns})^{-1}$ (see Fig. 8a). The applied excitation powers are the same as used in the main text for observing the variations in the bunching visibility. Although the intrinsic lifetime of an exciton commonly deviates from a mono-exponential fit in a cascade recombination, we employed the average exciton decay rates considering that their variations versus pump power were negligible ($\Delta\Gamma = \pm 0.05\ (\mathrm{ns})^{-1}$). We

also note that the $XX_{\mathrm{L}}X_{\mathrm{R}}$, $X_{\mathrm{L}}X_{\mathrm{R}}$ and X_{R} lifetimes comply with the ordering required for their cascaded nature[14], i.e. $\Gamma_{XX_{\mathrm{L}}X_{\mathrm{R}}} > \Gamma_{X_{\mathrm{L}}X_{\mathrm{R}}} > \Gamma_{X_{\mathrm{R}}}$.

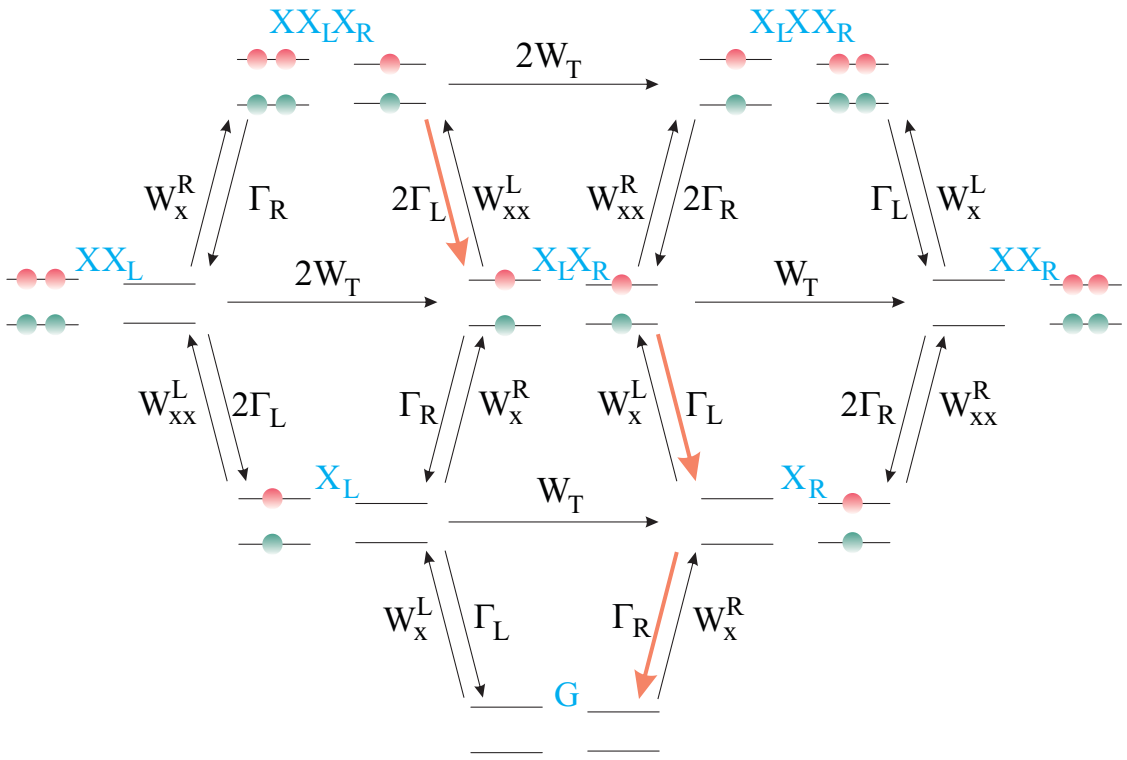

Figure 7: The energy level structure of the excitons, biexcitons and triexciton in a QDM. Upward, downward and horizontal arrows denote excitation, decay and direct energy transfer rates, respectively. The red thick arrows show the $XX_{\mathrm{L}}X_{\mathrm{R}}$, $X_{\mathrm{L}}X_{\mathrm{R}}$ and X_{R} transitions in the main text.

We accounted for the direct energy transfer (Förster transfer) of excitons among the two s shells as characterized by $\mathrm{W_T}$ in the diagram. Förster transfer originates from long-range interdot Coulomb interactions[22] and its rate depends on several parameters including energy difference of QDM s shells ($\Delta E = E_{X_{\mathrm{L}}} - E_{X_{\mathrm{R}}}$), interdot spacing and QDM symmetry[38]. Note that a sizeable interdot Coulomb coupling does not necessarily lead to the exciton Förster transfer, because the transfer matrix element in QDMs with broken symmetry greatly depends on ΔE and phonon as-

sisted mechanisms[38]. In practice, a direct energy transfer via the Förster coupling is likely between two molecular states in a relative resonance (< 5 meV)[23,38]. An energy separation equivalent to ~ 70 meV between the s-shell resonances of the smaller and larger dots excludes such a direct tunneling mechanism ($\mathrm{W_T} \approx 0$) in our QDM. We note that the s shell in $\mathrm{QD_L}$ is located in the vicinity of upper shells in $\mathrm{QD_R}$ (perhaps d shells), and this may promote the nonresonant carrier tunneling from the d shells of $\mathrm{QD_R}$ into the s shell of $\mathrm{QD_L}$ via phonon-assisted coupling. Under such conditions, the effective pumping rate of the s shell in $\mathrm{QD_L}$, $\mathrm{W_x^L}$, will dynamically increase as compared to $\mathrm{W_x^R}$.

The important parameters used to model the measured cross correlations in the main text are compiled in Table 1. The model is incapable of comprising the excitation power P_{exc} and the PL intensity of resonances. The influence of the incoherent pumping is reflected in the pump rate of transitions ($P_{\mathrm{exc}} \propto W_{\mathrm{P}}\hbar\omega_{\mathrm{P}}$ holds for a typical laser transition, however we repudiate such exact proportionality for quantum dot transitions). We found that $\mathrm{W_{xx}^L}$ or $\mathrm{W_{xx}^R}$ cannot grow fast and must be sufficiently smaller than $\mathrm{W_x^L}$ or $\mathrm{W_x^R}$, to precisely fit to the bunching peaks of $XX_{\mathrm{L}}X_{\mathrm{R}}$-$X_{\mathrm{L}}X_{\mathrm{R}}$ and $XX_{\mathrm{L}}X_{\mathrm{R}}$-$X_{\mathrm{R}}$ measured correlation. For simplicity, we presumed $\mathrm{W_{xx}^L} = \mathrm{W_{xx}^R}$ but their ratio can be similar to $\mathrm{W_x^L/W_x^R}$. As inferred from Table 1, $\mathrm{W_x^L}$ and $\mathrm{W_x^R}$ are enhanced super-linearly while $\mathrm{W_{xx}^L}$ and $\mathrm{W_{xx}^R}$ grow linearly, which agrees with our method of power amplification in practice (see Methods). It is not feasible to pinpoint the exact values of pumping rates due to the many parameters involved and the approximative nature of our model. The impact of detector was introduced into the correlations through convolving them with a Guassian lineshape: $f = 1/\sqrt{2\pi\sigma_{\mathrm{D}}}\exp(-t^2/2\sigma_{\mathrm{D}}^2)$, where $\sigma_{\mathrm{D}} = 250$ ps is the APD temporal resolution.

Table 1: Parameters used to produce the cross correlation curves in Fig. 8. W_x^L, W_x^R, W_{xx}^L and W_{xx}^R are chosen to fit the numerical curves to the experimental data, whereas $\Gamma_{X_L X_R}$ and Γ_{X_R} are measured experimentally.

Curve Num.	W_x^L (ns^{-1})	W_x^R (ns^{-1})	W_{xx}^L (ns^{-1})	W_{xx}^R (ns^{-1})	$\Gamma_{X_L X_R}(ns^{-1})$	$\Gamma_{X_R}(ns^{-1})$
1	0.97	0.24	0.20	0.20	0.838 ± 0.05	0.643 ± 0.05
2	1.18	0.33	0.21	0.21	0.898 ± 0.05	0.633 ± 0.05
3	1.57	0.55	0.23	0.23	0.934 ± 0.05	0.555 ± 0.05
4	2.15	0.84	0.26	0.26	0.950 ± 0.05	0.549 ± 0.05
5	2.89	1.20	0.30	0.30	0.907 ± 0.05	0.563 ± 0.05
6	3.77	1.64	0.31	0.31	0.897 ± 0.05	0.561 ± 0.05
7	4.57	2.03	0.32	0.32	0.900 ± 0.05	0.576 ± 0.05
8	5.74	3.85	0.34	0.34	0.879 ± 0.05	0.586 ± 0.05

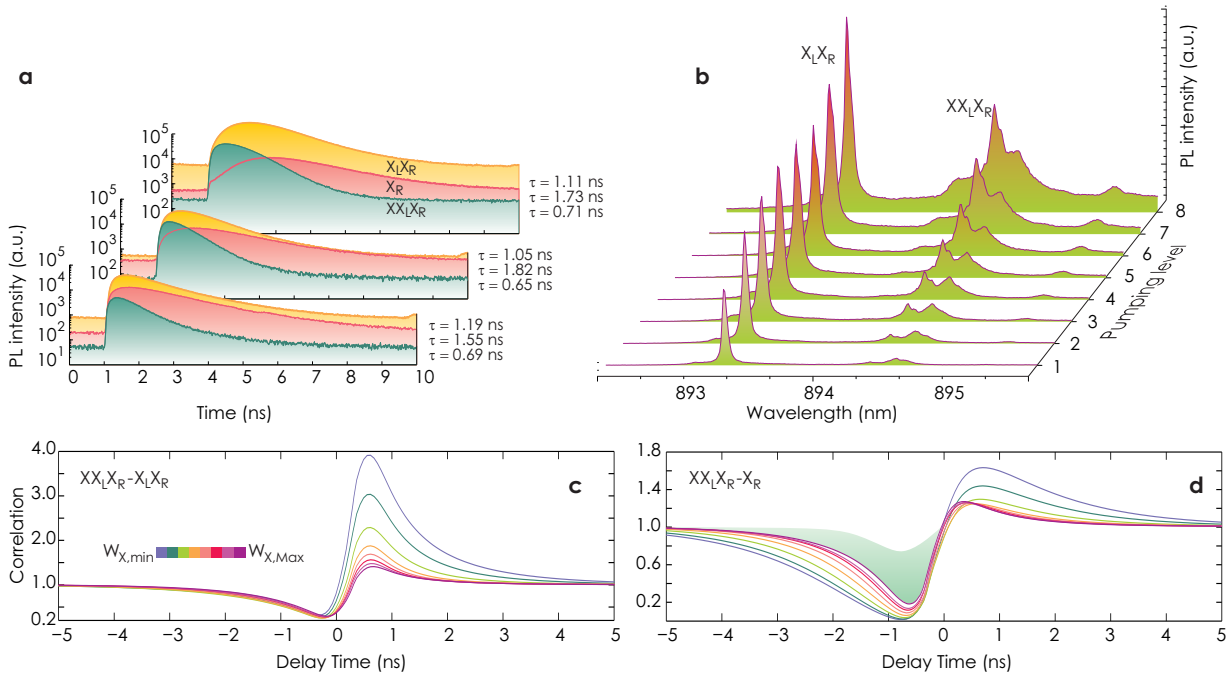

Figure 8: a) The time-resolved PL intensity of X_{R}, $X_{\mathrm{L}}X_{\mathrm{R}}$ and $XX_{\mathrm{L}}X_{\mathrm{R}}$ resonances displayed for the first, fourth and seventh spectra plotted in (b). The fitted lifetimes undergo an insignificant change even though elevating the excitation power leads the violation of the monoexponential fit. The output power of the pulsed laser is adjusted to reproduce the same spectra as seen in the cw mode in (b). The temporal resolution for the time-resolved measurement is set to 30 ps. b) The H.E. set spectra plotted for the eight quadratically increasing power densities starting from 220 $\mathrm{mW/mm^2}$. (c-d) The cross-correlations of $XX_{\mathrm{L}}X_{\mathrm{R}}$ resonance with $X_{\mathrm{L}}X_{\mathrm{R}}$ and X_{R} resonances calculated empirically using the time-propagation model. The curves are color-coded according to the excitation rates listed in 1. The green-shaded area shows the difference in the antibunching dip between the modeling and experimental data due to the excessive background light collected by the multimode fibre.

The model given above merely accounts for the radiative excitation of neutral states and neglects the formation of charged particles that can affect the neutrality of quantum dots through nonradiative mechanisms. Moreover, the model does not directly incorporate the PL intensity of spectral lines. However, putting the accuracy of parameters aside, the model is qualitatively

in a very good agreement with our experimental results approving the suppression of bunching visibility of a triple cascade in QDMs.

Triple coincidence counts To further clarify the peculiarities seen in the triple coincidence histogram plotted in Fig. 3d in the main text, we simulated the three-photon correlations numerically. To comply with the observations, we assumed that $XX_{\mathrm{L}}X_{\mathrm{R}}$ serves as the Start signal while $X_{\mathrm{L}}X_{\mathrm{R}}$ and X_{R} function as Stop1 and Stop2, respectively. The temporal characteristics are treated consistent with the experiment. We model three different scenarios: first, three uncorrelated single photon sources of the same brightness and recombination energy as $XX_{\mathrm{L}}X_{\mathrm{R}}$, $X_{\mathrm{L}}X_{\mathrm{R}}$ and X_{R} are considered. Poissonian noise on every individual channel was taken into account to mimic a realistic counting experiment. The triple coincidence histogram is plotted in Fig. 9(a), where fully random contributions from the three photons form the background level (by average 319 counts). In the second (third) case, we correlate the measured twofold coincidences of $XX_{\mathrm{L}}X_{\mathrm{R}}$ and $X_{\mathrm{L}}X_{\mathrm{R}}$ (X_{R}) with uncorrelated X_{R} ($X_{\mathrm{L}}X_{\mathrm{R}}$) signal. The outcome reproduces the so-called "bunching walls" superimposed on top of the fully accidental events, see Fig. 9(b-c). These features are partially correlated and clearly observed as the dual-channel bunching along τ_{31} and τ_{21} axes in Fig. 3d in the main text. The third bunching wall in the experimental plot (not simulated here) originates from twofold correlations of $X_{\mathrm{L}}X_{\mathrm{R}}$ and X_{R} with $XX_{\mathrm{L}}X_{\mathrm{R}}$ being random. The threefold coincidence peak sits at the intersection of these three bunching features.

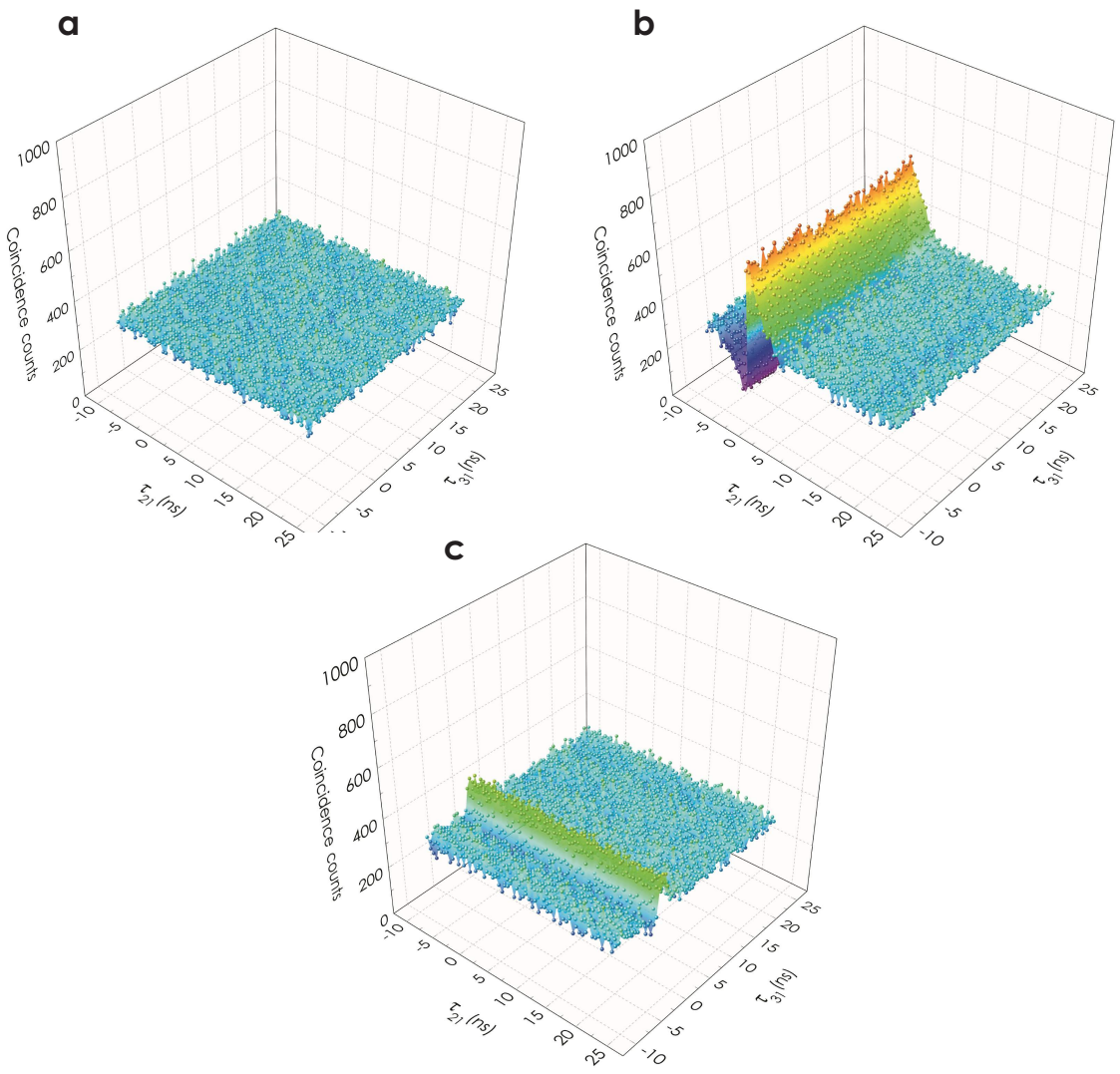

Figure 9: Simulated triple coincidence counts: a) background level made of fully random contributions from three uncorrelated photons. b) Correlated $XX_{\mathrm{L}}X_{\mathrm{R}}$ and $X_{\mathrm{L}}X_{\mathrm{R}}$ with random contribution from X_{R}. c) Correlated $XX_{\mathrm{L}}X_{\mathrm{R}}$ and X_{R} with random contribution from $X_{\mathrm{L}}X_{\mathrm{R}}$.

References

1. Bouwmeester, D., Pan, J.-W., Daniell, M., Weinfurter, H. & Zeilinger, A. Observation of three-photon greenberger-horne-zeilinger entanglement. *Phys. Rev. Lett.* **82**, 1345–1349 (1999).

2. Eibl, M. *et al.* Experimental observation of four-photon entanglement from parametric down-conversion. *Phys. Rev. Lett.* **90**, 200403 (2003).

3. Zhao, Z. *et al.* Experimental demonstration of five-photon entanglement and open-destination teleportation. *Nature* **430**, 54–58 (2004).

4. Yao, X.-C. *et al.* Observation of eight-photon entanglement. *Nature Photonics* **6**, 225–228 (2012).

5. Hübel, H. *et al.* Direct generation of photon triplets using cascaded photon-pair sources. *Nature* **466**, 601–603 (2010).

6. Hamel, D. R. *et al.* Direct generation of three-photon polarization entanglement. *Nature Photonics* **8**, 801–807 (2014).

7. Rauschenbeutel, A. Step-by-step engineered multiparticle entanglement. *Science* **288**, 2024–2028 (2000).

8. Pan, J.-W., Daniell, M., Gasparoni, S., Weihs, G. & Zeilinger, A. Experimental demonstration of four-photon entanglement and high-fidelity teleportation. *Phys. Rev. Lett.* **86**, 4435–4438 (2001).

9. Greve, K. D. *et al.* Quantum-dot spin–photon entanglement via frequency downconversion to telecom wavelength. *Nature* **491**, 421–425 (2012).

10. Bayer, M. *et al.* Coupling and entangling of quantum states in quantum dot molecules. *Science* **291**, 451–453 (2001).

11. Guerreiro, T. *et al.* Nonlinear interaction between single photons. *Phys. Rev. Lett.* **113**, 173601 (2014).

12. Moreau, E. *et al.* Quantum cascade of photons in semiconductor quantum dots. *Phys. Rev. Lett.* **87**, 183601 (2001).

13. Jayakumar, H. *et al.* Time-bin entangled photons from a quantum dot. *Nature Communications* **5**, 4251 (2014).

14. Persson, J., Aichele, T., Zwiller, V., Samuelson, L. & Benson, O. Three-photon cascade from single self-assembled InP quantum dots. *Phys. Rev. B* **69**, 233314 (2004).

15. Schmidgall, E. R. *et al.* Deterministic generation of a quantum-dot-confined triexciton and its radiative decay via three-photon cascade. *Phys. Rev. B* **90**, 241411(R) (2014).

16. Stevenson, R. M. *et al.* A semiconductor source of triggered entangled photon pairs. *Nature* **439**, 179–182 (2006).

17. Huber, T. *et al.* Polarization entangled photons from quantum dots embedded in nanowires. *Nano Letters* **14**, 7107–7114 (2014).

18. Bleuse, J. *et al.* Inhibition, enhancement, and control of spontaneous emission in photonic nanowires. *Phys. Rev. Lett.* **106**, 103601 (2011).

19. Stinaff, E. A. Optical signatures of coupled quantum dots. *Science* **311**, 636–639 (2006).

20. Gawarecki, K., Pochwała, M., Grodecka–Grad, A. & Machnikowski, P. Phonon-assisted relaxation and tunneling in self-assembled quantum dot molecules. *Phys. Rev. B* **81**, 245312 (2010).

21. Bester, G., Shumway, J. & Zunger, A. Theory of excitonic spectra and entanglement engineering in dot molecules. *Phys. Rev. Lett.* **93**, 047401 (2004).

22. Govorov, A. O. Spin and energy transfer in nanocrystals without tunneling. *Phys. Rev. B* **68**, 075315 (2003).

23. Rozbicki, E. & Machnikowski, P. Quantum kinetic theory of phonon-assisted excitation transfer in quantum dot molecules. *Phys. Rev. Lett.* **100**, 027401 (2008).

24. Stavrou, V. N. & Hu, X. Electron relaxation in a double quantum dot through two-phonon processes. *Phys. Rev. B* **73**, 205313 (2006).

25. Beirne, G. J. *et al.* Quantum light emission of two lateral tunnel-coupled (In,Ga)As/GaAs quantum dots controlled by a tunable static electric field. *Phys. Rev. Lett.* **96**, 137401 (2006).

26. Khaetskii, A. V. & Nazarov, Y. V. Spin relaxation in semiconductor quantum dots. *Phys. Rev. B* **61**, 12639–12642 (2000).

27. Witek, B. J. *et al.* Measurement of the g-factor tensor in a quantum dot and disentanglement of exciton spins. *Phys. Rev. B* **84**, 195305 (2011).

28. Bayer, M., Walck, S. N., Reinecke, T. L. & Forchel, A. Exciton binding energies and diamagnetic shifts in semiconductor quantum wires and quantum dots. *Phys. Rev. B* **57**, 6584–6591 (1998).

29. Santori, C., Fattal, D., Vučković, J., Solomon, G. S. & Yamamoto, Y. Indistinguishable photons from a single-photon device. *Nature* **419**, 594–597 (2002).

30. Gerardot, B. D. *et al.* Photon statistics from coupled quantum dots. *Phys. Rev. Lett.* **95**, 137403 (2005).

31. Lahmam-Bennani, A., Dupré, C. & Duguet, A. Electron-impact double ionization of argon studied by double and triple coincidence techniques: The first (e, 3e) experiment. *Phys. Rev. Lett.* **63**, 1582–1585 (1989).

32. Reimer, M. E. *et al.* Bright single-photon sources in bottom-up tailored nanowires. *Nature Communications* **3**, 737 (2012).

33. Kuroda, T. *et al.* Bunching visibility for correlated photons from single GaAs quantum dots. *Phys. Rev. B* **79**, 035330 (2009).

34. Eibl, M., Kiesel, N., Bourennane, M., Kurtsiefer, C. & Weinfurter, H. Experimental realization of a three-qubit entangled w state. *Phys. Rev. Lett.* **92**, 077901 (2004).

35. Waks, E. *et al.* Secure communication: Quantum cryptography with a photon turnstile. *Nature* **420**, 762–762 (2002).

36. Dalacu, D. *et al.* Ultraclean emission from InAsP quantum dots in defect-free wurtzite InP nanowires. *Nano Letters* **12**, 5919–5923 (2012).

37. Dalacu, D. *et al.* Selective-area vapour–liquid–solid growth of InP nanowires. *Nanotechnology* **20**, 395602 (2009).

38. Govorov, A. O. Spin-förster transfer in optically excited quantum dots. *Phys. Rev. B* **71**, 155323 (2005).